

# Common cause for severe droughts in South America and marine heatwaves in the South Atlantic

Regina R. Rodrigues<sup>1\*</sup>, Andréa S. Taschetto<sup>2</sup>, Alex Sen Gupta<sup>2</sup> and Gregory R. Foltz<sup>3</sup>

**In 2013/14 eastern South America experienced one of its worst droughts. At the same time an unprecedented marine heatwave developed in the western South Atlantic. The drought was linked to suppression of the South Atlantic convergence zone and its associated rainfall, which led to water shortages in Brazil and impacted food supplies globally. Here we show from observations that such droughts and adjacent marine heatwaves have a common remote cause. Atmospheric blocking triggered by tropical convection in the Indian and Pacific oceans can cause persistent anticyclonic circulation that not only leads to severe drought but also generates marine heatwaves in the adjacent ocean. We show that increased shortwave radiation due to reduced cloud cover and reduced ocean heat loss from weaker winds are the main contributors to the establishment of marine heatwaves in the region. The proposed mechanism, which involves droughts, extreme air temperature over land and atmospheric blocking explains approximately 60% of the marine heatwave events in the western South Atlantic. We also identified an increase in frequency, duration, intensity and extension of marine heatwave events over the satellite period 1982–2016. Moreover, surface primary production was reduced during these events with implications for regional fisheries.**

The establishment of the South Atlantic convergence zone (SACZ) during austral summer characterizes the South American monsoon system and is the source of rainfall to eastern South America<sup>1</sup>. The SACZ is a band of strong precipitation oriented northwest–southeast, from the Amazon towards the western South Atlantic (Fig. 1a) and is associated with a cyclonic circulation over eastern South America that channels moisture from the Amazon towards southeast Brazil<sup>2</sup>. This region is heavily populated, home to more than 80 million people, and responsible for 60% of the Brazilian gross domestic product. Failure in the development of the SACZ in the summer can lead to water, food and power shortages, as occurred during the drought in the summer of 2013/14 (Fig. 1a)<sup>3</sup>. This event was responsible for a dengue fever outbreak that tripled the usual number of fatalities<sup>4</sup>. It also led to water shortages in São Paulo, the world's fourth most populated city<sup>3,5,6</sup> and reduced Brazilian coffee production, which led to global shortages and worldwide price increases<sup>7</sup>.

The massive scale of this drought event sparked interest from the scientific community, which led to a number of studies dedicated to explaining the origins of this episode. The picture that emerged was that a persistent anticyclonic circulation established over southeast Brazil both prevented synoptic systems reaching the region and inhibited the development of the SACZ and its associated rainfall<sup>3,5,6,8,9</sup>. The anticyclonic circulation, in turn, was a result of wave-breaking events over subtropical South America with similar characteristics to mid-latitude atmospheric blocking<sup>10</sup>. This mechanism is not exclusive to the summer of 2013/14. For the period 1979–2014, the years with more blocking days typically coincide with the years with fewer SACZ days and less precipitation<sup>10</sup>. However, the persistence (duration) of the blocking event was remarkable in 2013/14 and also led to an intense heatwave<sup>11</sup> (Fig. 1b). Furthermore, the northerly

wind anomalies on the western flank of the anticyclonic circulation acted to intensify the South American low-level jet, which carried moisture from the Amazon to southeastern South America and led to floods in southern Brazil, Uruguay and northern Argentina<sup>11</sup> (Fig. 1a).

## An unprecedented marine heatwave in the South Atlantic

Interestingly, an unusually hot episode of similar magnitude and large extent co-occurred in the adjacent ocean but went largely unnoticed by the scientific community. A severe marine heatwave (MHW) developed in the South Atlantic during the summer of 2013/14. Sea surface temperatures (SSTs) reached up to 3°C above climatological averages for large areas of the western South Atlantic (Fig. 1b,c) and lasted for almost all of the summer (Supplementary Fig. 1). MHWs are analogues to atmospheric heatwaves and have important consequences for marine life<sup>12</sup>. They are defined as prolonged periods of anomalously high SST<sup>13</sup> and can be classified as moderate, strong, severe or extreme<sup>14</sup> (Methods). Various prominent events in the global ocean were identified, such as those in the Mediterranean Sea in 2003<sup>15</sup>, off western Australia in 2011<sup>16</sup>, in the northwest Atlantic in 2012<sup>17</sup>, in the northeast Pacific in 2014/15<sup>18</sup> and in the Tasmanian Sea in 2015/16<sup>19</sup>. These events had devastating consequences, which ranged from extensive coral bleaching<sup>20</sup>, mass mortality of marine organisms and changes in community structure<sup>19,21</sup> to fisheries closures and quota changes<sup>19,22</sup>. The MHW event in the western South Atlantic in 2013/14 was responsible for a decrease in surface chlorophyll *a* levels that pushed the concentrations two standard deviations below average over a large area of the western South Atlantic (Fig. 1d and Supplementary Fig. 2). Understanding the physical processes behind the genesis of such MHWs is crucial for predicting them and their impacts on marine life and coastal resources, but to date there are no studies on the

<sup>1</sup>Department of Oceanography, Federal University of Santa Catarina, Florianópolis, Brazil. <sup>2</sup>Climate Change Research Centre and ARC Centre of Excellence for Climate Extremes, University of New South Wales, New South Wales, Sydney, Australia. <sup>3</sup>NOAA/Atlantic Oceanographic and Meteorological Laboratory, Miami, FL, USA. \*e-mail: [regina.rodrigues@ufsc.br](mailto:regina.rodrigues@ufsc.br)

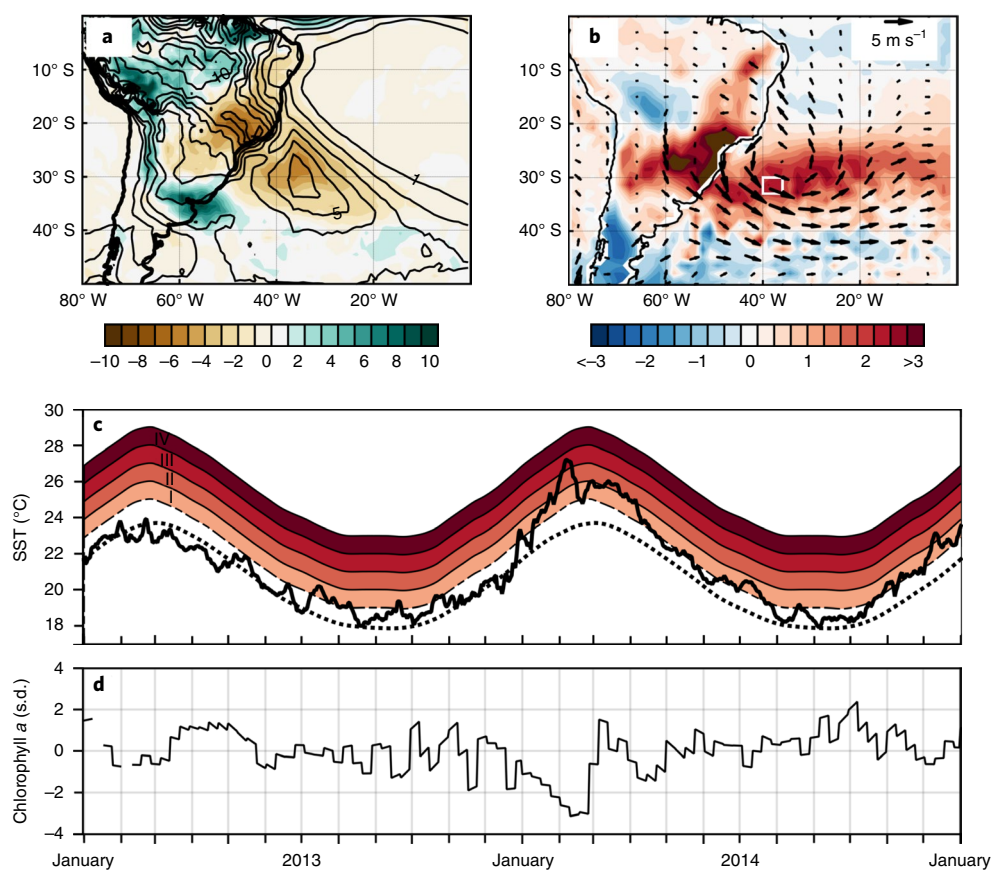


**Fig. 1 | The 2013/14 western South Atlantic MHW event. a**, Anomalies of precipitation averaged for the period from 15 January 2013 to 13 February 2014 (colour shading (mm d<sup>-1</sup>)). Contours display the climatological mean precipitation with contour intervals of 1 mm d<sup>-1</sup>. **b**, As in **a**, but for anomalies of average sea surface and air temperature (°C) and surface wind vectors. **c**, Time series of observed SST (black thick line), the long-term regional climatology (dotted line) and the 90th percentile climatology (dashed line). MHW severity categories I–IV are shown in shades of red: I, moderate; II, strong; III, severe; IV, extreme. **d**, Time series of surface chlorophyll *a* concentration (in mg m<sup>-3</sup>) normalized by its s.d. The time series in **c** and **d** are averaged over the box 30–33° S and 36–40° W shown in **b**.

mechanisms of the 2013/14 MHW or MHWs in the South Atlantic in general.

Here we identify a common atmospheric pattern that persists during western South Atlantic MHWs. First, we applied a standardized methodology to identify all the MHW events during austral summer for the period 1982–2016<sup>13,14</sup>. The mean signature of the SST warming for all the events is similar to that of the 2013/14 event (Fig. 2a). The anomalous anticyclonic circulation, a hallmark of atmospheric blocking, is also evident during these events (Fig. 2a). The time series of atmospheric blocking days per summer<sup>10</sup> is strongly correlated to the SST anomalies for the same area of the western South Atlantic, with coefficients as high as 0.7 (Fig. 2b) corroborating our hypothesis that, as for the 2013/14 MHW, atmospheric blocking over subtropical South America is linked to ocean warming. Although blocking conditions persist for about 18% of the time, up to 60% of MHW days occur simultaneously with atmospheric blocking days (Fig. 2c). Furthermore, the same proportion of extreme air temperatures (defined as days when the air temperature is above the 95th percentile) also occurs during atmospheric blocking events (Fig. 2d).

### A common remote trigger for regional droughts and MHWs

The anomalous anticyclonic circulation that characterizes the blocking appears as part of a stationary Rossby wave train that emanates from a deep convection in the western Pacific/maritime continent over warm SST<sup>8,9</sup>. More recently, the origin of the

atmospheric perturbations was shown to lie in the deep convection mainly over the Indian Ocean associated with the Madden–Julian Oscillation (MJO), when daily data are considered<sup>10</sup>. Indeed, the second mode of a maximum covariance analysis (MCA) of daily outgoing longwave radiation (OLR) anomalies over the tropical belt (30° S to 30° N) and the SST anomaly in the western South Atlantic (0–60° W, 10–50° S) for austral summer clearly shows an enhanced convection over the Indian Ocean (Fig. 3a) in association with a SST pattern reminiscent of the MHW events (Fig. 3c; the first mode is associated with El Niño Southern Oscillation, not shown). The OLR pattern (Fig. 3a) looks very similar to phase 2 of the MJO, which is associated with enhanced convection in the eastern Indian Ocean. Moreover, the MJO is active during 92.6% of the MHW days that occur simultaneously with atmospheric blocking days, and 20% of those days correspond to MJO phase 2 (Supplementary Table 1 gives more details). The maximum values of the SST principal component (PC) time series occurred during the summer of 2013/14 (Fig. 3b).

In addition, composites of geopotential anomalies in the upper troposphere (200 hPa) for the MHWs that coincide with atmospheric blocking show Rossby wave trains that emanate from the Indian Ocean (Fig. 3d, colour shading), travelling through the atmospheric jet (Fig. 3d, solid lines) to reach subtropical South America and establish the blocking anticyclone approximately six days later (Fig. 3e). The complete evolution of the teleconnection pattern is given in Supplementary Fig. 3, obtained from two different data sets

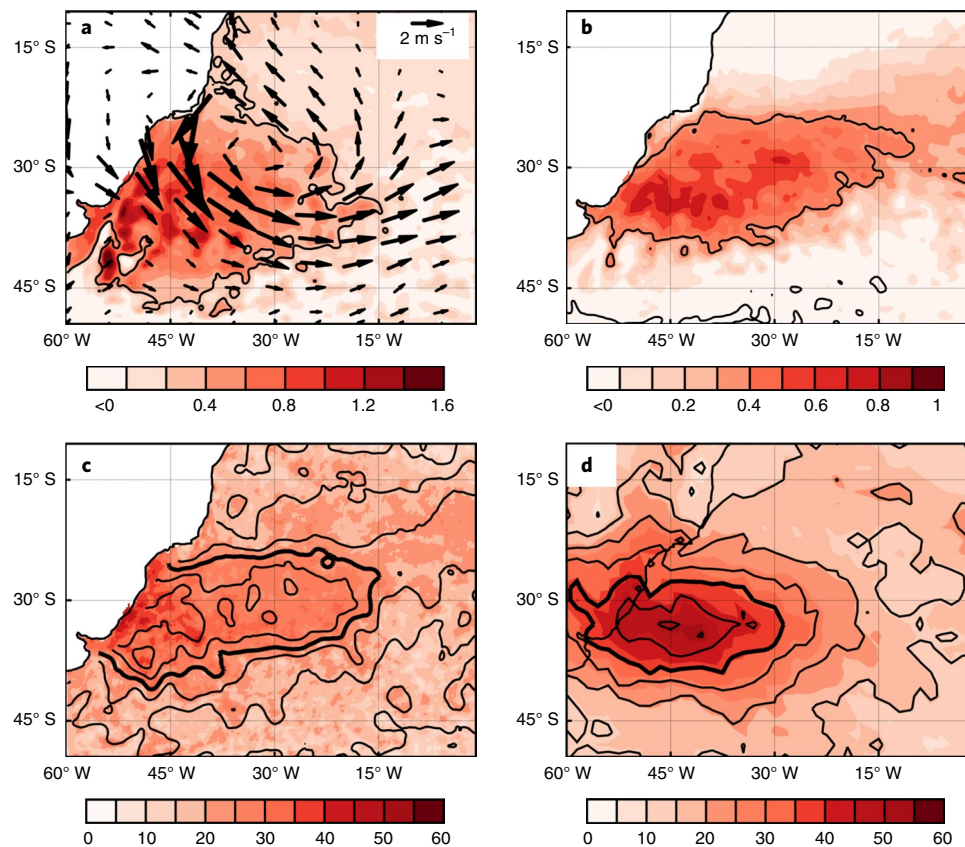


**Fig. 2 | Western South Atlantic MHW during austral summer for the period 1982–2016.** **a**, Composite of SST anomalies (colour shading ( $^{\circ}\text{C}$ )) and surface wind anomalies (vectors) for MHW events. **b**, Correlation between time series of the SST anomalies and atmospheric blocking over subtropical South America. **c**, Percentage of MHW days that occurred simultaneously with blocking for each grid point. **d**, As in **c**, but for extremes of air temperature. The contours in **a** and **b** enclose areas where the composite and the correlation coefficient, respectively, are statistically significant at a 95% confidence level. The contours in **c** and **d** are the total number of synchronized MHWs and air temperature extreme days, respectively, with the contour interval every 20 days; the bold contour represents the 100-day isoline.

to show the robustness of our results. We also computed the Rossby wave source (RWS) to identify the origin of variability associated with the MHW events (Methods). The RWS can be used to examine the mechanisms by which the mid-latitude circulation responds to changes associated with tropical convection. Regions of strong RWS represent the locations of wave train excitations. In the case of MHW events they occur along the jet stream over the Indian Ocean sector (cyan contours in Fig. 3d) poleward of  $30^{\circ}\text{S}$  because upper-level convergence is observed at the descending branch of the Hadley cell around  $30^{\circ}\text{S}$ , associated with the upper-level divergence caused by convection along the tropics. Also notable is that, even though the jet is stronger along the whole Indian Ocean (contours in Fig. 3d), it is closer to the equator in the eastern side of the basin. Thus, convection in the eastern Indian Ocean associated with MJO phase 2 is more likely to propagate along the jet, which acts as a waveguide.

### Local processes involved in the MHW generation

Once the anticyclone is established, the MHW is generated by local changes in the heat fluxes between the ocean and the atmosphere. This can be seen from the evolution of the 2013/14 MHW event (Fig. 4a–i). The anticyclonic circulation is associated with convergence in the upper levels and subsidence (not shown) that suppresses convection (Fig. 4a,d) and consequently the establishment of the SACZ. The associated decrease in cloud cover increases shortwave radiation (SWR) at the ocean's surface (Fig. 4a,d). Latent heat loss from the ocean to the atmosphere (evaporative cooling) decreases

(positive anomalies in Fig. 4b,e) due to the combined effect of weak winds and enhanced moisture transport from the South America low-level jet to the MHW area, which saturates the air above the MHW (Fig. 4c,f). The ocean warms (contours in Fig. 4e) and the MHW reaches its peak. Note that the increase in SWR affects the northeastern portion of the MHW, whereas the reduced latent heat loss is confined to the southern part of the MHW. Changes in shortwave generate the largest changes, similar to that found for the 2014/15 MHW in the northeast Pacific<sup>23</sup>. In the decay phase, another anticyclone that approaches from the southwest brings cooler and drier air to the MHW area and drastically enhances the evaporative cooling (Fig. 4g–i). As a consequence, the MHW event comes to an abrupt end. The composites averaged during all the MHWs show a similar evolution, albeit with weaker anomalies during the establishment of other MHWs (Supplementary Fig. 4). The other heat flux terms, longwave radiation (LWR) and sensible heat flux (SHF), are of lesser importance (Supplementary Fig. 4). These results were also reproduced using another data set (Supplementary Figs. 5 and 6). A recent study also shows that the MJO can cause a warming of the western South Atlantic due to surface heat fluxes<sup>24</sup>.

To quantify the local processes that contribute to the MHW generation, we calculated the temperature budget of the ocean mixed layer (Methods). The time series of the temperature budget components averaged within the  $30^{\circ}\text{S}$ – $33^{\circ}\text{S}$ ,  $36^{\circ}\text{W}$ – $40^{\circ}\text{W}$  region are shown in Fig. 4j for the period from January 2013 to December 2014. The rate of change of the mixed-layer temperature

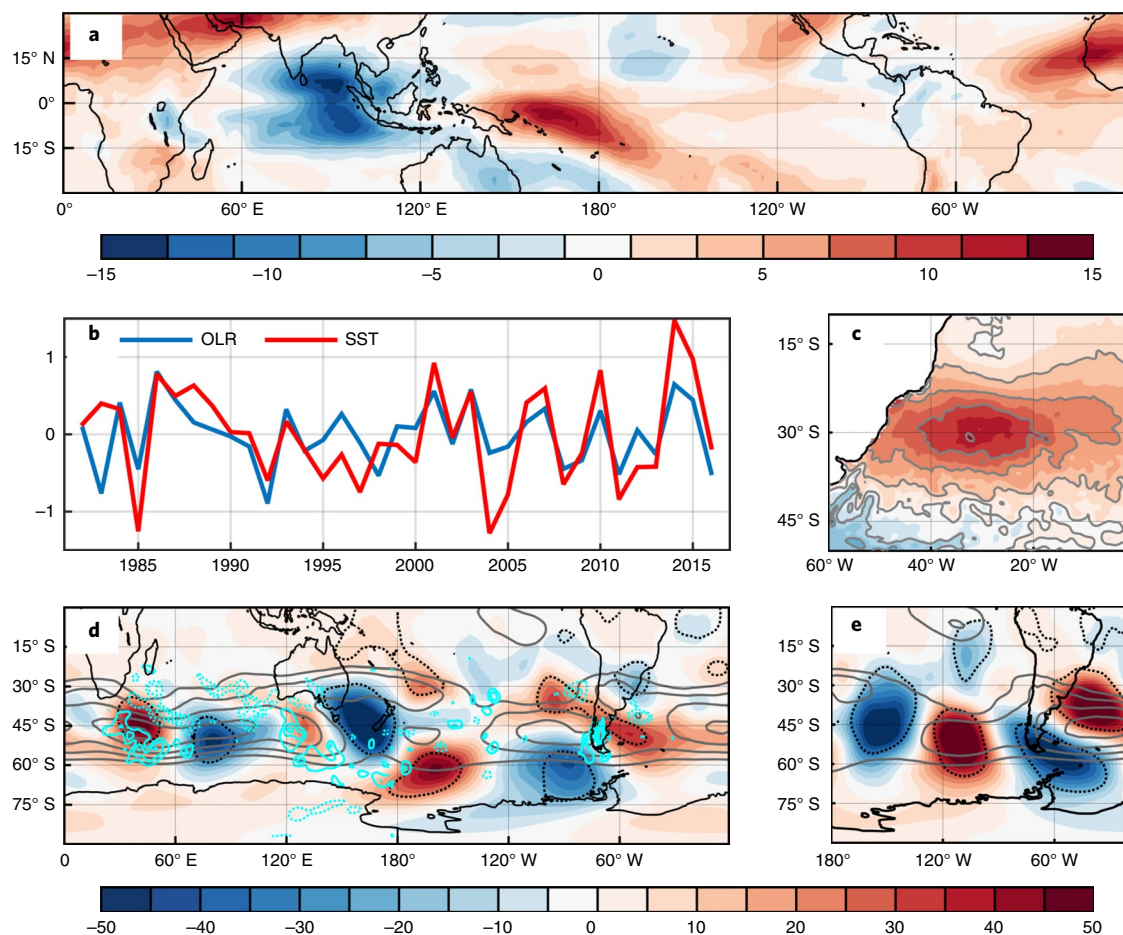


**Fig. 3 | Precursor of atmospheric blocking and MHWs.** **a, c**, The second mode patterns from the MCA of OLR (**a**) and SST (**c**) for austral summer. Contour intervals are  $0.2^{\circ}\text{C}$  in **c**. **b**, The PC time series of OLR and SST. The seasonal means are plotted. **d**, Time-lagged composites of geopotential height anomalies (colour shading (m)) and zonal wind (grey solid contours ( $\text{m s}^{-1}$ )) at 200 hPa for 6 days prior to the onset of the subtropical South Atlantic blocking events in austral summer that were followed by a MHW event in the South Atlantic. **e**, as in **d**, but at the onset day. RWS anomalies are displayed in cyan in **d** ( $\times 10^{-9} \text{ s}^{-2}$ ); solid and dashed contours represent, respectively, the positive and negative RWS anomalies. The contour intervals are  $5 \text{ m s}^{-1}$ , starting at  $20 \text{ m s}^{-1}$ , and  $1 \times 10^{-9} \text{ s}^{-2}$  starting at  $\pm 2 \times 10^{-9} \text{ s}^{-2}$ . Black dotted contours encompass areas in which the anomalies of geopotential are statistically significantly different from the climatology at the 95% confidence level.

( $\partial T/\partial t$ ) is dominated by SWR during the development of the main MHW event (January to February of 2014) associated with the reduction in clouds and by latent heat flux (LHF) during the decay of the event. Consistent with our qualitative analysis (Supplementary Figs. 4 and 6), the LWR and SHF terms are of less importance. The zonal and meridional advection terms are negligible. Importantly, the difference between the sum of all the components and the rate of change of the mixed layer temperature (derived from independent data sources) is small (Supplementary Fig. 7). This residual represents the combination of unresolved processes, such as vertical turbulent diffusion or observational error, and its smallness suggests a robust result. These findings are insensitive to the choice of the domain as the results are very similar when the temperature budget is calculated for different regions within the study area (Supplementary Fig. 8). Moreover, this result also holds for other MHW events that occurred during the period 1998–2016 for which the temperature budget is calculated (Supplementary Fig. 9).

### Changes in the characteristics of the MHWs

The complete picture that emerges is depicted in a schematic (Fig. 5). Tropical deep convection and the related wind convergence in the eastern Indian Ocean associated with the passage of

the MJO ultimately lead to atmospheric blocking over the western South Atlantic as part of a planetary Rossby wave train. This, in turn, affects the local heat fluxes, winds and precipitation, and leads to drought and both terrestrial and marine heatwaves. Hopefully, understanding the mechanisms by which MHWs occur will help to predict them in the near- and long-term future. For short timescales, there is the potential for MHW predictability from MJO-related tropical convection, as was shown for the North Atlantic Oscillation<sup>25</sup>. To help understand future changes, we also need to know if the occurrence of these MHW events has varied over the recent decades. It is difficult to address this question because of the short length of reliable SST records in the South Atlantic. Nonetheless, there is an increase not only in frequency but also in duration, intensity and extension of MHW events over the satellite period 1982–2016 (Supplementary Fig. 10 and Supplementary Table 2). For instance, there was an increase of 8.4 MHW days per year per decade when widespread MHW events are considered (when the SSTs surpass the threshold of over more than 50% of the area between  $30^{\circ}\text{--}35^{\circ}\text{S}$  and  $30^{\circ}\text{--}50^{\circ}\text{W}$ ). Given that 25 and 10% of the area yields an increase of 12 and 15.6 MHW days per year per decade, respectively. The MHW events are on average 18 days per decade longer and  $0.05^{\circ}\text{C}$  per decade more intense with an increase in their total areal extent of 7% per decade.

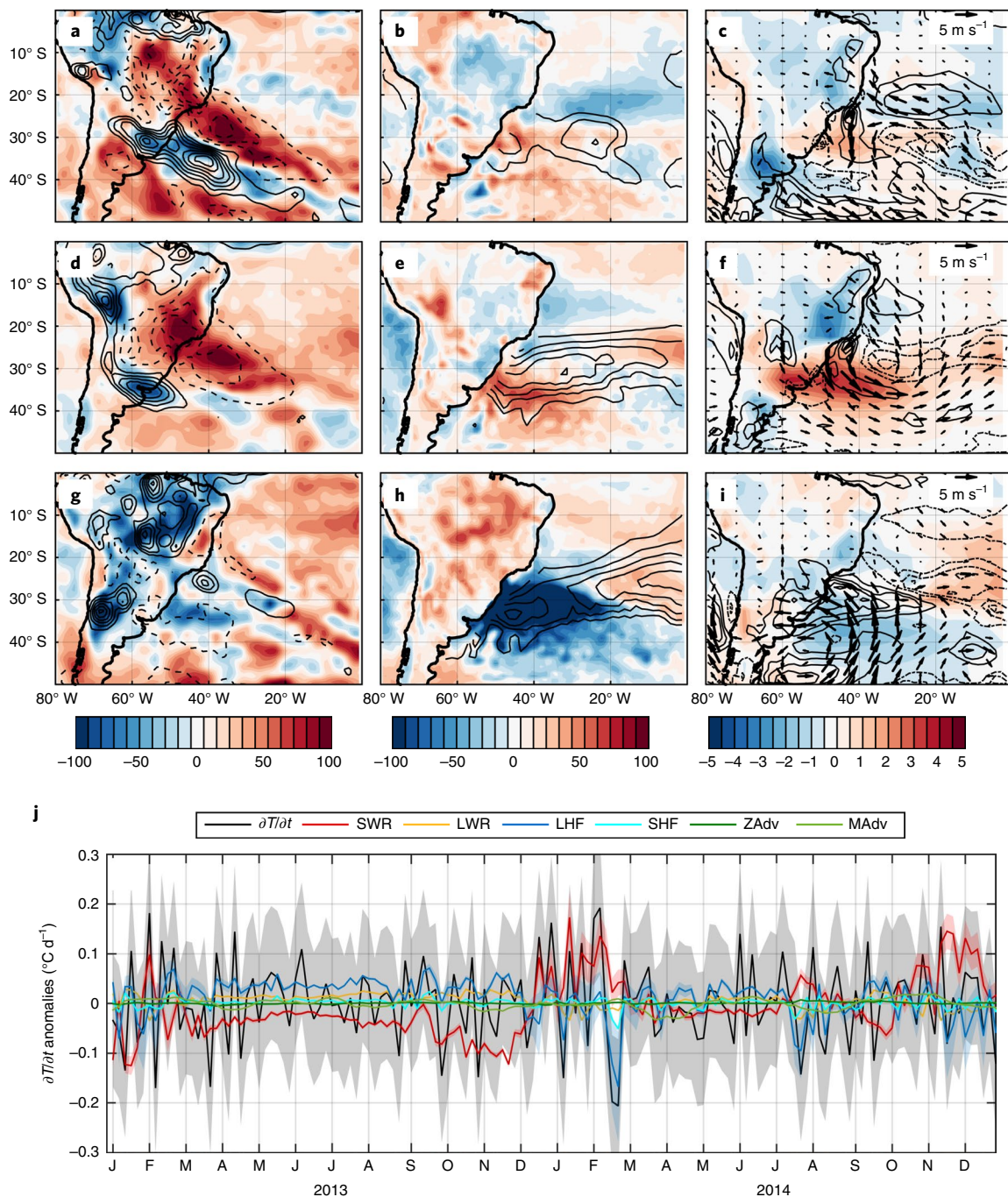


**Fig. 4 | Mechanism of onset and decay of the 2013/2014 MHW event.** Composites of anomalies. **a**, SWR (colours shading ( $\text{W m}^{-2}$ )) and precipitation (contours ( $\text{mm d}^{-1}$ )). **b**, LHF (colour shading ( $\text{W m}^{-2}$ )) and SST (contours ( $^{\circ}\text{C}$ )). **c**, Specific humidity (colour shading ( $\text{g kg}^{-1}$ )), wind (vectors) and wind speed (contours ( $\text{m s}^{-1}$ )) during the week before the 2013/14 event onset. **d-f**, As in **a-c** but during the peak of the 2013/14 event. **g-i**, As in **a-c** but during the week after the 2013/14 event peak. Contour intervals are every  $2 \text{ mm d}^{-1}$  in **a**, **d** and **g**, every  $0.5 \text{ }^{\circ}\text{C}$  in **b**, **e** and **h** and every  $1 \text{ m s}^{-1}$  in **c**, **f** and **i**. In all the panels, the positive (negative) anomalies are displayed with solid (dashed) contours and zero contours are omitted. **j**, Temperature budget averaged in the  $30\text{--}33^{\circ}\text{S}$ ,  $36\text{--}40^{\circ}\text{W}$  region; contours show the time series of the individual components (rate of change of SST, shortwave, longwave, latent, sensible, zonal (ZAdv) and meridional temperature advection (MAAdv)); shaded grey area represents the error bar associated with each component (Methods).

All the aforementioned trends are statistically significant at the 99% confidence level using the non-parametric Mann–Kendall test and are consistent with global average trends<sup>26,27</sup>. Note that the PC time series of the OLR and SST MCA (Fig. 3b) are significantly correlated with the time series of MHW frequency, duration, intensity and duration (Supplementary Fig. 10 and Supplementary Table 3).

Some of the remaining questions to be answered are: (1) can the aforementioned changes be attributed to natural or anthropogenic causes and (2) will they be more frequent in the future? Regarding the first question, there is some evidence that the changes in tropical deep convection in the Indian Ocean and a SST pattern similar to that found here for MHWs related to MJO events are modulated by the Interdecadal Pacific Oscillation<sup>10,28,29</sup> and thus that changes

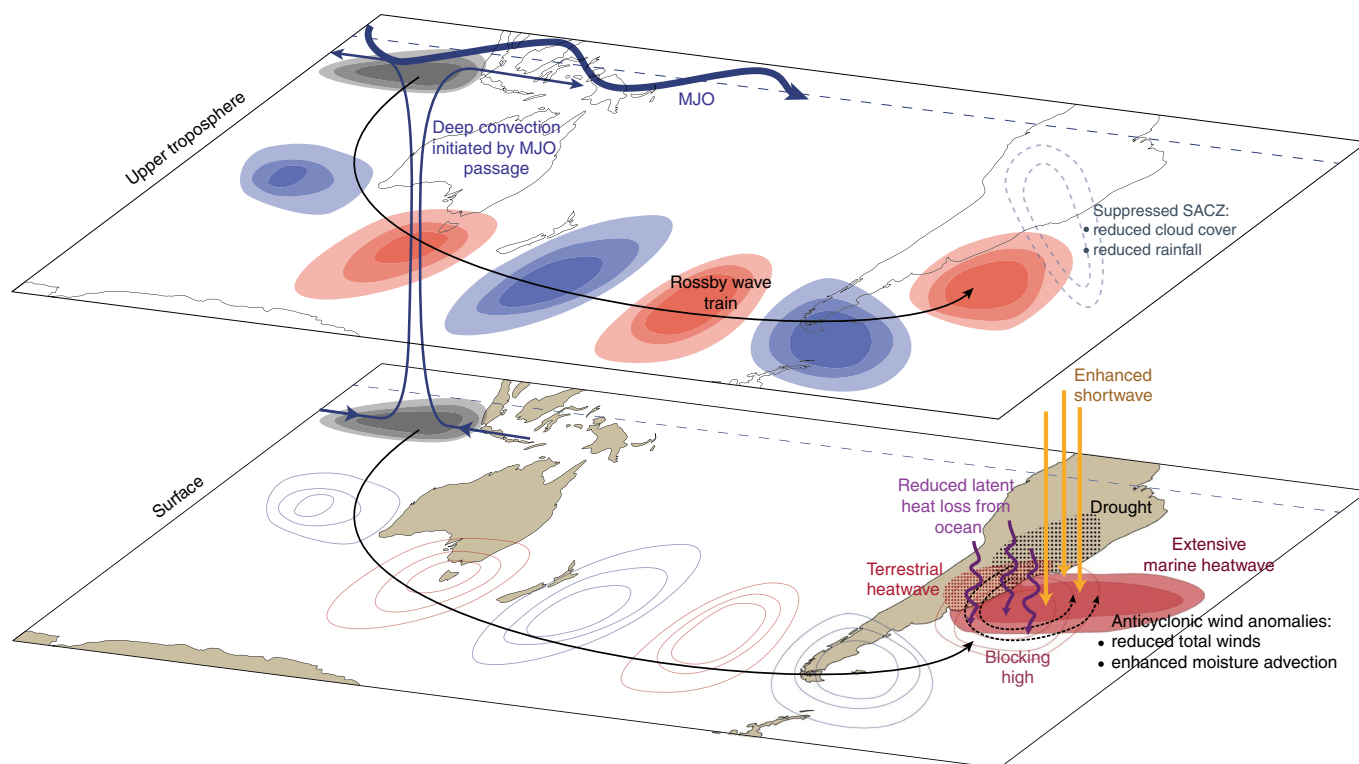


**Fig. 5 | Schematic representation of the forcing mechanisms of the western South Atlantic MHWs.** Tropical deep convection, mainly in the Indian Ocean, associated with the MJO passage triggers a Rossby wave train that extends through the South Pacific to the tip of South America and turns equatorward to reach subtropical South America. There a blocking anticyclone is established that suppresses the SACZ, reducing cloud cover and precipitation. This, in turn, increases the input of shortwave radiation into the ocean. At the same time, latent heat loss from the ocean is reduced due to weaker winds and enhanced moisture advection. Heat is retained in the ocean, which leads to extensive MHWs.

in the MHWs can be attributed to natural decadal changes. We also note that neither blocking nor MHWs are significantly correlated with the El Niño–Southern Oscillation or the Southern Annular Mode, the two leading modes of natural climate variability in the Southern Hemisphere. The occurrence of blocking and MHWs (Supplementary Fig. 10) is very low during major El Niño events (1982/83, 1997/98 and 2015/16) and La Niña events (1984/85, 1988/89 and 1999/2000). In relation to the second question as to whether MHWs will become more frequent, a recent study<sup>27</sup> shows that under global warming MHWs in the global oceans, including the South Atlantic, will be longer lasting and more frequent, extensive and intense. Therefore, it is possible that the positive trends observed in the intensity, frequency and persistence of MHWs in the region will continue as the world warms. To address this question, a more detailed study of western South Atlantic MHWs is underway using a suite of Earth system model simulations.

### Online content

Any methods, additional references, Nature Research reporting summaries, source data, statements of code and data availability and associated accession codes are available at <https://doi.org/10.1038/s41561-019-0393-8>.

Received: 29 March 2019; Accepted: 24 May 2019;  
Published online: 8 July 2019

### References

- Marengo, J. A. et al. Recent developments on the South American monsoon system. *Int. J. Climatol.* **32**, 1–21 (2012).
- Carvalho, L. M., Jones, C. & Liebmann, B. The South Atlantic convergence zone: intensity, form, persistence, and relationships with intraseasonal to interannual activity and extreme rainfall. *J. Clim.* **17**, 88–108 (2004).
- Getirana, A. C. V. Extreme water deficit in Brazil detected from space. *J. Hydrometeorol.* **17**, 591–599 (2015).
- BBC. Brazil faces surge in number of dengue fever cases *BBC News* [www.bbc.com/news/world-latin-america-32589268](http://www.bbc.com/news/world-latin-america-32589268) (5 May 2015).
- Coelho, C. A. S., Cardoso, D. H. F. & Firpo, M. A. F. Precipitation diagnostics of an exceptionally dry event in São Paulo, Brazil. *Theor. Appl. Climatol.* **125**, 769–784 (2016).
- Otto, F. E. L. et al. Factors other than climate change, main drivers of 2014/15 water shortage in southeast Brazil. *Bull. Am. Meteorol. Soc.* **96**, S35–S40 (2015).
- Watson, K. Drought hits Brazil's coffee industry *BBC News* [www.bbc.com/news/business-27623535](http://www.bbc.com/news/business-27623535) (30 May 2014).
- Coelho, C. A. S. et al. The 2014 southeast Brazil austral summer drought: regional scale mechanisms and teleconnections. *Clim. Dyn.* **46**, 3737–3752 (2015).
- Seth, A., Fernandes, K. & Camargo, S. J. Two summers of São Paulo drought: origins in the western tropical Pacific. *Geophys. Res. Lett.* **42**, 10816–10823 (2015).
- Rodrigues, R. R. & Woollings, T. Impact of atmospheric blocking on South America in austral summer. *J. Clim.* **30**, 1821–1837 (2017).
- Sánchez-Lugo, A. South America [in “State of the Climate in 2014”]. *Bull. Am. Meteorol. Soc.* **96**, S178–S184 (2015).
- Smale, D. A. et al. Marine heatwaves threaten global biodiversity and the provision of ecosystem services. *Nat. Clim. Change* **9**, 306–312 (2019).
- Hobday, A. J. et al. A hierarchical approach to defining marine heatwaves. *Prog. Oceanogr.* **141**, 227–238 (2016).
- Hobday, A. J. et al. Categorizing and naming marine heatwaves. *Oceanography* **31**, 162–173 (2018).
- Sparnocchia, S., Schiano, M. E., Picco, P., Bozzano, R. & Cappelletti, A. The anomalous warming of summer 2003 in the surface layer of the Central Ligurian Sea (Western Mediterranean). *Ann. Geophys.* **24**, 443–452 (2006).
- Pearce, A. F. & Feng, M. The rise and fall of the ‘marine heat wave’ off Western Australia during the summer of 2010/11. *J. Mar. Syst.* **112**, 139–156 (2013).
- Chen, K., Gawarkiewicz, G. G., Lentz, S. J. & Bane, J. M. Diagnosing the warming of the Northeastern US Coastal Ocean in 2012: a linkage between the atmospheric jet stream variability and ocean response. *J. Geophys. Res. Ocean* **119**, 218–227 (2014).

18. Di Lorenzo, E. & Mantua, N. Multi-year persistence of the 2014/15 North Pacific marine heatwave. *Nat. Clim. Change* **6**, 1042–1047 (2016).
19. Oliver, E. C. J. et al. The unprecedented 2015/16 Tasman Sea marine heatwave. *Nat. Commun.* **8**, 16101 (2017).
20. Hughes, T. P. et al. Global warming and recurrent mass bleaching of corals. *Nature* **543**, 373–377 (2017).
21. Garrabou, J. et al. Mass mortality in Northwestern Mediterranean rocky benthic communities: effects of the 2003 heat wave. *Glob. Change Biol.* **15**, 1090–1103 (2009).
22. Cavole, L. M. et al. Biological impacts of the 2013–2015 warm-water anomaly in the Northeast Pacific: winners, losers, and the future. *Oceanography* **29**, 273–285 (2016).
23. Myers, T. A., Mechoso, C. R., Cesana, G. V., DeFlorio, M. J. & Waliser, D. E. Cloud feedback key to marine heatwave off Baja California. *Geophys. Res. Lett.* **45**, 4345–4352 (2018).
24. Barreiro, M. et al. Modelling the role of Atlantic air–sea interaction in the impact of Madden–Julian Oscillation on South American climate. *Int. J. Climatol.* **39**, 1104–1116 (2019).
25. Cassou, C. Intraseasonal interaction between the Madden–Julian oscillation and the North Atlantic Oscillation. *Nature* **455**, 523–527 (2008).
26. Oliver, E. C. et al. Longer and more frequent marine heatwaves over the past century. *Nat. Commun.* **9**, 1324 (2018).
27. Frölicher, T. L., Fischer, E. M. & Gruber, N. Marine heatwaves under global warming. *Nature* **560**, 360–364 (2018).
28. Nieves, V., Willis, J. K. & Patzert, W. C. Recent hiatus caused by decadal shift in Indo-Pacific heating. *Science* **349**, 532–535 (2015).
29. Lopez, H., Dong, S., Lee, S.-K. & Campos, E. Remote influence of Interdecadal Pacific Oscillation on the South Atlantic meridional overturning circulation variability. *Geophys. Res. Lett.* **43**, 8250–8258 (2016).

## Acknowledgements

R.R.R. is supported by CNPq (no. 401873/2016-1) and CAPES (no. 88881.145866/2017-1). A.S. and A.S.T. (FT160100495) are supported by the Australian Research Council. This work is part of the research conducted by the Programmes INCT-MCII (CNPq no. 465501/2014-1 and CAPES/FAPS no. 16/2014) and Rede CLIMA (FINEP no. 01.13.0353-00). G.R.F. was supported by base funds to NOAA/AOML.

## Author contributions

The main idea was developed by R.R.R. in collaboration with A.S.T. and A.S. Most of the text was written by R.R.R., who also did the data preparations and most of the data analyses and made the figures. G.R.F. provided the temperature budget calculations. The schematic was prepared by A.S. All the authors contributed with ideas, discussed the results and implications and contributed to the text.

## Competing interests

The authors declare no competing interests.

## Additional information

**Supplementary information** is available for this paper at <https://doi.org/10.1038/s41561-019-0393-8>.

**Reprints and permissions information** is available at [www.nature.com/reprints](http://www.nature.com/reprints).

**Correspondence and requests for materials** should be addressed to R.R.R.

**Publisher's note:** Springer Nature remains neutral with regard to jurisdictional claims in published maps and institutional affiliations.

© The Author(s), under exclusive licence to Springer Nature Limited 2019

## Methods

**Data sets.** To identify the MHW events in this study, we used daily gridded SST data obtained from the National Oceanic and Atmospheric Administration Optimum Interpolation Sea Surface Temperature V2.0<sup>30</sup> with a horizontal resolution of 1/4° for the period 1982–2016. To compute the wave-breaking index and the composites of the atmospheric variables, we used data obtained from the European Centre for Medium-Range Weather Forecasts ERA-Interim reanalysis<sup>31</sup> for the same period. Daily values were obtained by averaging the 6 h data of the potential temperature on the tropopause, zonal and meridional components of the wind at the surface and at 850 hPa, geopotential height at 200 hPa, 2 m air temperature and surface specific humidity. Shortwave and longwave radiative fluxes and sensible and latent turbulent heat fluxes were also obtained from the same data set. However, their daily values were calculated by averaging the 12 h forecast outputs. We also used the gridded daily rainfall data provided by the Global Precipitation Climatology Project with a horizontal resolution of 2.5° for the period 1997–2016<sup>32</sup> and the interpolated OLR daily data<sup>33</sup> as a proxy for tropical convection, with same spatial resolution for the period 1982–2016. The OLR MJO index<sup>34</sup> was obtained from the Physical Sciences Division (Earth System Research Laboratory of the National Oceanic and Atmospheric Administration) for the same period. Surface chlorophyll *a* data were obtained from weekly level-3 satellite images from SeaWiFS and Aqua-MODIS sensors with a horizontal resolution of 9 km for the period 2002–2016<sup>35</sup>. Additional data sets were used to calculate the mixed-layer temperature budget: 5 days Ocean Surface Current Analysis-Realtime (OSCAR) horizontal velocity that represents mean values in the upper 30 m of the ocean, calculated from satellite sea level, winds and SST and available on a 0.33° grid<sup>36</sup>; daily averages of LHF and SHF on a 1° grid from the Objectively Analysed air–sea Fluxes (OAFlux) data set<sup>37</sup>; downward SWR at the surface of the ocean is available from the Surface Solar Radiation Data Set Heliosat-2 (SARAH-2) on a 0.05° grid<sup>38</sup> and monthly ORAS4 temperature and salinity on a 1° grid<sup>39</sup>.

**Defining MHWs.** Following the standardized MHW definition<sup>13</sup>, a MHW event occurs when the SSTs exceed a seasonally varying 90th percentile for a minimum of five consecutive days. According to this methodology<sup>13</sup>, an event is considered continuous even if gaps of 2 days or less occur between events. Here we also calculated the severity of each MHW event using a simple categorization scheme<sup>14</sup>. Multiples of the 90th percentile difference from the mean climatology value define the MHW categories as: (I) moderate (1×), (II) strong (2×), (III) severe (3×) and (IV) extreme (4×). As an example for the area in the western South Atlantic between 30–33° S and 36–40° W, Fig. 1c shows the time series of observed SSTs (bold line), the long-term regional climatology (dashed line), the 90th percentile climatology (thin line) and the MHW categories I–IV (tones of red) from 01 January 2013 to 31 December 2014.

**Defining atmospheric blocking.** Here we used the same methodology as described in previous studies<sup>10,40,41</sup> to compute an instantaneous two-dimensional wave-breaking index based on the reverse of the meridional potential temperature on the tropopause (–2 PV units) for the domain within 25 and 75° S. Boxes with dimensions of 15° latitude by 5° longitude are defined to the south and north of each central location and the potential temperature is averaged over these areas. A large-scale measure of the meridional potential temperature gradient is given by subtracting the northern box average from the southern box average. Then, a wave-breaking episode is said to occur at a specific longitude when large-scale wave breaking is detected within 10° of the longitude of it for a minimum duration of four consecutive days. Wave-breaking episode frequency is defined as the percentage of days when a wave-breaking episode occurs within a specific season. We defined the area of the subtropical South America blocking by taking all the grid points in this sector when the mean wave-breaking frequency was above 5% during austral summer<sup>10</sup>. Note that here we include March in our analyses for austral summer because this month presents a high number of blocking frequency that surpasses the December value. For the period 1982–2016, the summer blocking frequency was 18% (763 days of a possible 4,244 days).

**MCA and RWS.** To identify the source of variability, we performed a MCA of daily OLR anomalies over the tropical belt (30° N to 30° S) and SST anomaly within the western South Atlantic (0°–60° W, 10–50° S) for all the summers (December, January, February and March) for the period 1982–2016<sup>42</sup>. The MCA provides the dominant spatial patterns of covariability between the two fields. We also calculated RWS using the formulation described in previous studies<sup>10,43</sup>. RWS is defined as  $-\nabla \cdot (\mathbf{v}_z \cdot \boldsymbol{\zeta})$  where  $\mathbf{v}_z$  is the divergent component of the horizontal velocity field at 200 hPa and  $\boldsymbol{\zeta}$  is the absolute vorticity. Strong RWS occurs in the jet stream regions where large gradients in vorticity occur poleward of the diabatic tropical heating.

**Mixed-layer temperature budget.** Here the mixed-layer temperature budget of the ocean is defined as  $dT/dt = -\mathbf{v} \cdot \nabla T + Q_0/\rho C_p h + \delta$ , where  $\rho$  is the density of seawater (1,025 kg m<sup>-3</sup>),  $C_p$  is the specific heat of seawater (3,940 J kg<sup>-1</sup> K<sup>-1</sup>),  $T$  is temperature and  $\mathbf{v}$  is the horizontal velocity vector, both vertically averaged over

the mixed layer,  $Q_0$  is the net surface heat flux, which includes LHF and SHF, SWR absorbed in the mixed layer and net LWR emission,  $h$  is the mixed layer depth (MLD) and  $\delta$  represents unresolved processes such as vertical turbulent diffusion. The rate of change of mixed-layer temperature  $dT/dt$  is calculated using daily averages of the SST because previous studies have shown that SST agrees very well with the mixed-layer temperature<sup>44</sup>. The horizontal temperature advection (first term on the right) is calculated as the sum of the SST transport (using the daily interpolated OSCAR horizontal velocity) around the boundaries of the region between 30–33° S and 36–40° W relative to the SST averaged in the region<sup>45</sup>. For the net surface heat flux (second term on the right), we used daily averages of LHF and SHF from OAFlux and daily downward LWR from ERA-Interim. LWR emitted by the ocean is calculated as  $\epsilon \sigma T^4$ , where  $\epsilon$  is the emissivity (0.97),  $\sigma$  is the Stefan–Boltzmann constant and  $T$  is the SST. Downward SWR at the surface of the ocean is available from SARAH-2 and agrees very well with direct measurements from moorings in the tropical Atlantic<sup>46</sup>. We applied an albedo of 6% and then calculated the amount of SWR that penetrated through the base of the mixed layer using an algorithm<sup>47,48</sup> based on satellite chlorophyll *a* concentrations from SeaWiFS. The MLD, required for the calculation of penetrative SWR and  $Q_0$ , was estimated using the criterion of a 0.07 kg m<sup>-3</sup> density increase from a depth of 5 m, obtained from monthly ORAS4 temperature and salinity. The monthly MLD was then interpolated to daily values to calculate the heat flux terms. All the temperature budget terms were calculated for the period 1998–2016 and averaged in the 30–33° S, 36–40° W region. Anomalies were calculated using the 1998–2016 daily climatology. Uncertainties for each term were calculated<sup>49</sup> using daily errors of 10 m for MLD, 10 W m<sup>-2</sup> for LWR, 20 W m<sup>-2</sup> for surface SWR, 0.3 °C for SST and 8 cm s<sup>-1</sup> for horizontal velocity. Error estimates for LHF and SHF are provided in the OAFlux data set.

**Statistical analysis.** In this study, the statistical significance of the composites and correlations was evaluated using a Monte Carlo test, randomly selecting the same number of days from the climatological sample, taking into account the data autocorrelation timescale. This process is repeated 10,000 times and grid points where either the composite mean or the correlation coefficient is in the most extreme 5% of their surrogated counterparts are considered significant. The non-parametric test of Mann–Kendall is used for the trends. The panels in Fig. 1 were obtained from averaging the fields for the longest event of atmospheric blocking for the period 1982–2016. To construct the composites of SST anomalies in Fig. 2a, we used all the days in which the severity averaged over the area between 30–35° S and 30–50° W was above 1.5. We tested the sensitivity of our choice by using the criteria of averaged severity above 1.0 and 1.2 and the warming pattern did not change considerably, albeit the anomalies were weaker (not shown). For the composites shown in Fig. 3, we first determined the MHW events that occurred simultaneously with atmospheric blocking and defined the first day of these simultaneous events as the onset day.

## Data availability

The SST and atmospheric data used in this work are freely available from [www.esrl.noaa.gov/psd/data/gridded/data.noaa.oisst.v2.highres.html](http://www.esrl.noaa.gov/psd/data/gridded/data.noaa.oisst.v2.highres.html) and <http://apps.ecmwf.int/datasets/data/interim-full-daily/levtype=sfc/>, respectively. The precipitation and OLR data are provided freely at [www.esrl.noaa.gov/psd/data/gridded/](http://www.esrl.noaa.gov/psd/data/gridded/). The ocean colour data are also freely available from <https://oceancolor.gsfc.nasa.gov>. OSCAR currents are available from [https://podaac.jpl.nasa.gov/dataset/OSCAR\\_L4\\_OC\\_third-deg](https://podaac.jpl.nasa.gov/dataset/OSCAR_L4_OC_third-deg). Surface turbulent heat fluxes from OAFlux were obtained from <http://oafux.whoi.edu/data.html>. The SARAH-2 SWR data are available from [https://wui.cmsaf.eu/safira/action/viewDoiDetails?acronym=SARAH\\_V002\\_01](https://wui.cmsaf.eu/safira/action/viewDoiDetails?acronym=SARAH_V002_01). Ocean data from ORAS4 are available from [www.ecmwf.int/en/research/climate-reanalysis/ocean-reanalysis](http://www.ecmwf.int/en/research/climate-reanalysis/ocean-reanalysis).

## References

- Reynolds, R. W. et al. Daily high-resolution-blended analyses for sea surface temperature. *J. Clim.* **20**, 5473–5496 (2007).
- Dee, D. P. et al. The ERA-Interim reanalysis: configuration and performance of the data assimilation system. *Q. J. R. Meteorol. Soc.* **137**, 553–597 (2011).
- Huffman, G. J. et al. Global precipitation at one-degree daily resolution from multisatellite observations. *J. Hydrometeorol.* **2**, 36–50 (2001).
- Liebmann, B. & Smith, C. A. Description of a complete (interpolated) outgoing longwave radiation dataset. *Bull. Am. Meteorol. Soc.* **77**, 1275–1277 (1996).
- Kiladis, G. N. et al. A comparison of OLR and circulation-based indices for tracking the MJO. *Mon. Weather Rev.* **142**, 1697–1715 (2014).
- Hu, C., Lee, Z. & Franz, B. Chlorophyll *a* algorithms for oligotrophic oceans: a novel approach based on three-band reflectance difference. *J. Geophys. Res. Oceans* **117**, C01011 (2012).
- Bonjean, F. & Lagerloef, G. S. E. Diagnostic model and analysis of the surface currents in the tropical Pacific Ocean. *J. Phys. Oceanogr.* **32**, 2938–2954 (2002).
- Yu, L. S. & Weller, R. A. Objectively analyzed air–sea heat fluxes for the global ice-free oceans (1981–2005). *Bull. Am. Meteorol. Soc.* **88**, 527–539 (2007).

38. Pfeifroth, U. et al. *Surface Radiation Data Set – Heliosat (SARAH) – Edition 2* (Satellite Application Facility on Climate Monitoring, 2017); [https://doi.org/10.5676/EUM\\_SAF\\_CM/SARAH/V002](https://doi.org/10.5676/EUM_SAF_CM/SARAH/V002)
39. Balmaseda, M. A., Mogensen, K. & Weaver, A. T. Evaluation of the ECMWF ocean reanalysis system ORAS4. *Q. J. R. Meteorol. Soc.* **139**, 1132–1161 (2013).
40. Berrisford, P., Hoskins, B. J. & Tyrllis, E. Blocking and Rossby wave breaking on the dynamical tropopause in the Southern Hemisphere. *J. Atmos. Sci.* **64**, 2881–2898 (2007).
41. Pelly, J. L. & Hoskins, B. J. A new perspective on blocking. *J. Atmos. Sci.* **60**, 743–755 (2003).
42. Bretherton, C. S., Smith, C. & Wallace, J. M. An intercomparison of methods for finding coupled patterns in climate data. *J. Clim.* **5**, 541–560 (1992).
43. Sardeshmukh, P. D. & Hoskins, B. J. The generation of global rotational flow by steady idealized tropical divergence. *J. Atmos. Sci.* **45**, 1228–1251 (1988).
44. Foltz, G. R., Grodsky, S. A., Carton, J. A. & McPhaden, M. J. Seasonal mixed layer heat budget of the tropical Atlantic Ocean. *J. Geophys. Res. Oceans* **108**, 3146 (2003).
45. Lee, T., Fukumori, I. & Tang, B. Temperature advection: internal versus external processes. *J. Phys. Oceanogr.* **34**, 1936–1944 (2004).
46. Trolliet, M. et al. Downwelling surface solar irradiance in the tropical Atlantic Ocean: a comparison of reanalyses and satellite-derived data sets to PIRATA measurements. *Ocean Sci.* **14**, 1021–1056 (2018).
47. Morel, A. & Antoine, D. Heating rate within the upper ocean in relation to its bio-optical state. *J. Phys. Oceanogr.* **24**, 1652–1665 (1994).
48. Sweeney, C. et al. Impacts of shortwave penetration depth on large-scale ocean circulation and heat transport. *J. Phys. Oceanogr.* **35**, 1103–1119 (2005).
49. Foltz, G. R., Schmid, C. & Lumpkin, R. An enhanced PIRATA data set for tropical Atlantic Ocean–atmosphere research. *J. Clim.* **31**, 1499–1524 (2018).